

# Imaging of Love Waves and Their Interaction with Magnetic Domain Walls in Magnetolectric Magnetic Field Sensors

Cai Müller, Phillip Durdaut, Rasmus B. Holländer, Anne Kittmann, Viktor Schell, Dirk Meyners, Michael Höft, Eckhard Quandt, and Jeffrey McCord\*

The complex behavior of horizontally polarized surface shear waves in magnetolectric surface acoustic wave based magnetic field sensor devices is revealed by time-resolved magnetooptical microscopy with picosecond temporal and submicron spatial resolution. The imaging of the propagating waves in the magnetolectric composites is realized through the functional soft-magnetic layer by coupled magnetoelastic interactions. Partial surface wave reflections, wave front dephasing, and secondary wave generation occur, which originate from structures and magnetic domain walls. Closure domain structures bend and reflect the magnetic surface waves. Strain stimulated magnetic domain walls display dynamic periodic expansions, which propagate along the domain walls and change the magnetomechanical response also in the surrounding regions. The revealed spatial and temporally varying nondeterministic response restricts the noise performance of the surface acoustic wave based magnetic field sensors and thus confines the sensor's limit of detection. Magnetic time-resolved optical imaging is shown to be a powerful method for the operando characterization of magnetolectric devices and in-plane displacement surface acoustic wave fields that are not accessible by other methods.


magnetolectric sensor devices, based on a combination of piezoelectric-ferromagnetic materials.<sup>[4,5]</sup> This includes devices based on surface acoustic wave (SAW) excitation that combine a low detection limit, a high dynamic range, and a large bandwidth.<sup>[6–8]</sup> SAWs are acoustic modes that are confined to one surface of a sample, concentrating the energy of the wave near that surface. Devices based on SAWs may utilize Rayleigh, shear horizontal, Lamb, and Love waves.<sup>[9–11]</sup> Love waves are pure shear transverse polarized waves and are used in a variety of sensing applications, most often with an additional functional thin film sensitive to the desired stimulus.<sup>[12–14]</sup> In general, the functional layer reacts to changes of the sensed physical quantity by which the propagating wave becomes altered in amplitude and in velocity. Magnetoelastic delay line magnetic field sensors utilizing SAWs make use of ferromagnetic films with a high piezomagnetic constant.<sup>[5–8,15–20]</sup>

In such piezoelectric-ferromagnetic structures, ferromagnetic films coupled to SAWs are used as tunable magnetoelastic delay lines. The principle of the operation of SAW magnetic field sensors is based on the magnetoelastic  $\Delta E$  effect, which transfers into a change of the effective mechanical Young's modulus, respectively shear modulus of the wave propagating medium depending on the magnetic state of the

## 1. Introduction

Physical property and especially magnetic field measurements are relevant to a wide range of applications.<sup>[1]</sup> Applied magnetic field sensing relies, e.g., on magnetoresistance and Hall effect measurements.<sup>[2,3]</sup> Recent approaches for the detection of low frequency biomagnetic signals depend on composite

C. Müller, R. B. Holländer, J. McCord  
 Nanoscale Magnetic Materials and Magnetic Domains  
 Institute for Materials Science  
 Kiel University  
 Kaiserstr. 2, 24143 Kiel, Germany  
 E-mail: jmc@tf.uni-kiel.de

 The ORCID identification number(s) for the author(s) of this article can be found under <https://doi.org/10.1002/aelm.202200033>.

© 2022 The Authors. Advanced Electronic Materials published by Wiley-VCH GmbH. This is an open access article under the terms of the Creative Commons Attribution-NonCommercial-NoDerivs License, which permits use and distribution in any medium, provided the original work is properly cited, the use is non-commercial and no modifications or adaptations are made.

P. Durdaut, M. Höft  
 Microwave Engineering, Institute of Electrical Engineering and Information Technology  
 Kiel University  
 Kaiserstr. 2, 24143 Kiel, Germany  
 A. Kittmann, V. Schell, D. Meyners, E. Quandt  
 Inorganic Functional Materials  
 Institute for Materials Science  
 Kiel University  
 Kaiserstr. 2, 24143 Kiel, Germany  
 D. Meyners, M. Höft, E. Quandt, J. McCord  
 Kiel Nano, Surface and Interface Science (KINSIS)  
 Kiel University  
 Christian-Albrechts-Platz 4, 24118 Kiel, Germany

DOI: 10.1002/aelm.202200033

incorporated magnetostrictive layer.<sup>[21]</sup> Altering the orientation of magnetization with a magnetic field results in a field dependent change of the SAW phase velocity and, as a result, leads to a measurable phase shift in the delay line SAW devices. By this, local variations in the orientation of magnetization in the incorporated ferromagnetic films, which are a direct result of the underlying magnetic domain structure, may impact the magnetoelastic wave response of the magnetic field sensors.

Magnetic noise in magnetic sensors is often related to hysteretic magnetic domain wall activity,<sup>[22,23]</sup> magnetic anisotropy dispersion<sup>[24]</sup> and, more general, is linked to magnetic losses in the magnetic material. In the latter case, the fluctuation-dissipation theorem<sup>[25]</sup> addresses induced magnetization fluctuation noise to the response of the magnetic system to small perturbing forces.<sup>[26,27]</sup>

So far, also SAW magnetic field sensors suffer from inherent noise, whose origin is associated to the magnetic losses that impact the sensor's performance in terms of achievable limit of detection (LOD), which is related to the SAW sensor devices' external magnetic excitation.<sup>[28]</sup> With high phase sensitivities in the range of  $S_{PM} \approx 1000^\circ/\text{mT}$ , magnetic noise currently limits the LOD for low frequency magnetic field signals to values around  $\text{LOD}_{\text{SAW}} \approx 100 \text{ pT/Hz}^{0.5}$ .<sup>[8,28,29]</sup> This corresponds to the magnetic noise floor of the Love wave delay line sensors that varies with the magnetic bias field, magnetic field history, and applied electrical power.<sup>[28]</sup> Magnetic noise is also reported for other types of excited magnetolectric sensing devices.<sup>[30,31]</sup> The magnetic activation of the SAW device is purely magnetoelastic and magnetic field free in nature, where the magnetic processes are unidentified. Yet, comparing electrical and standard quasistatic magnetic measurements, a basic connection between magnetization reversal details and phase noise could be established.<sup>[28]</sup> Especially, magnetic domain processes were correlated to the manifold occurring noise phenomena. Yet, the exact cause of phase noise of magnetic origin in the non-saturated magnetic state remains unclear as the actual link between the micromagnetic domain features and the propagating SAWs is not known. To obtain an insight, spatiotemporal investigations of the actual surface wave behavior, including also the functional ferromagnetic layer's magnetic domain behavior at the frequency of device operation, are essential.

In general, temporal analyses of the acoustic field have been used to understand the complex dependence of SAW properties on, e.g., effects of anisotropic elasticity of media and interactions with inhomogeneities of the material,<sup>[32,33]</sup> but also for insights in general SAW sensor and filter performance relevant aspects. Methods employed for the characterization of the time dependent acoustic wave field are interferometry,<sup>[34,35]</sup> holography,<sup>[36]</sup> scanning probe microscopy,<sup>[37]</sup> and photoemission electron microscopy (PEEM) in piezoelectric media.<sup>[38,39]</sup> Yet, since for Love waves there is no strain normal to the surface standard, out-of-plane displacement sensitive techniques like Laser Doppler Vibrometry are only indirectly applicable.<sup>[40]</sup> Only photoelastic methods have demonstrated the possibility of imaging propagating shear waves.<sup>[41,42]</sup> Fundamental magnetodynamic phenomena in SAW based devices have been studied by PEEM and magnetooptics.<sup>[43,44]</sup> An overview of the various techniques for the observation of surface acoustic wave fields

is shown in Table T1 (Supporting Information). Some of these studies are dealing with frequencies in the GHz regime. For such high SAW frequencies manifold effects due to magnon-phonon interactions are expected.<sup>[45–48]</sup>

Here, the use of wide-field magneto-optical Kerr effect (MOKE) microscopy<sup>[49]</sup> with high temporal resolution to study local effects of SAW propagation in magnetolectric composite structures is demonstrated. As we show, a time-resolved magnetic imaging approach<sup>[50,51]</sup> allows for the investigation of the acoustic wave field by means of the probed local magnetic variations. In contrast to time-resolved scanning probe MOKE microscopy,<sup>[52]</sup> the wide-field imaging approach allows for easy large field of view imaging and for the direct correlation with the quasistatic magnetic domain structures that can be imaged simultaneously in the same microscope setup. By this, we further reveal that the propagating SAWs strongly interfere with details of the micromagnetic spin structure in complex and nonreproducible ways. The micromagnetic processes at the domain walls are identified and connected to magnetic losses and local irreversible magnetic processes. The revealed complicated interactions result in a deterioration of magnetic field sensor performance.

## 2. Results and Discussion

### 2.1. SAW Device and General Magnetoelastic Response Characteristics

The overall device scheme is sketched in **Figure 1a**. It is based on a ST-cut quartz substrate, where two interdigital transducer (IDT) electrode pairs form a delay line. A  $\text{SiO}_2$  guiding layer together with an amorphous magnetostrictive ferromagnetic ( $\text{Fe}_{90}\text{Co}_{10}$ )<sub>78</sub> $\text{Si}_{12}\text{B}_{10}$  film provides a concentration of the wave energy at the device surface. Details on the structure and the modes of operation of the SAW based magnetic field sensor device are described in ref. 8.

For a shear wave traveling in  $x$ -direction, with the corresponding wave vector  $k$  as depicted in **Figure 1a**, the dominant shear stress at the surface is  $\tau_{xy}$ . This relates to the shear strain  $\gamma_{xy}$  as

$$\tau_{xy} = 2G_{\text{gl}}\gamma_{xy} \quad (1)$$

with the shear modulus  $G_{\text{gl}}$  of the guiding layer. For the given SAW device, the Love wave reaches several micrometers in depth (Supporting Information **Figure S2**). The wave propagation leads to a time-varying stress-induced magnetic anisotropy contribution  $K_\sigma$  in the magnetic surface layer and therefore to a variation of the angle of magnetization  $\varphi$  relative to  $k$ , where  $K_\sigma$  favors the alignment of magnetization  $M$  under an angle  $\varphi = \pm\pi/4$  relative to  $k$ . Together with an induced uniaxial anisotropy  $K_u$  and a magnetic field  $H$  acting on the ferromagnetic layer a time-varying alignment of magnetization is defined. In this regard, an orthogonal alignment of  $K_u$  and the vector of wave propagation  $k$ , together with  $H$  applied perpendicular to  $k$ , the total magnetic energy density  $e_{\text{tot}}$  is

$$e_{\text{tot}} = K_\sigma \sin^2(\pi/4 - \varphi) + K_u \sin^2(\varphi) + \mu_0 H M \cos \varphi \quad (2)$$

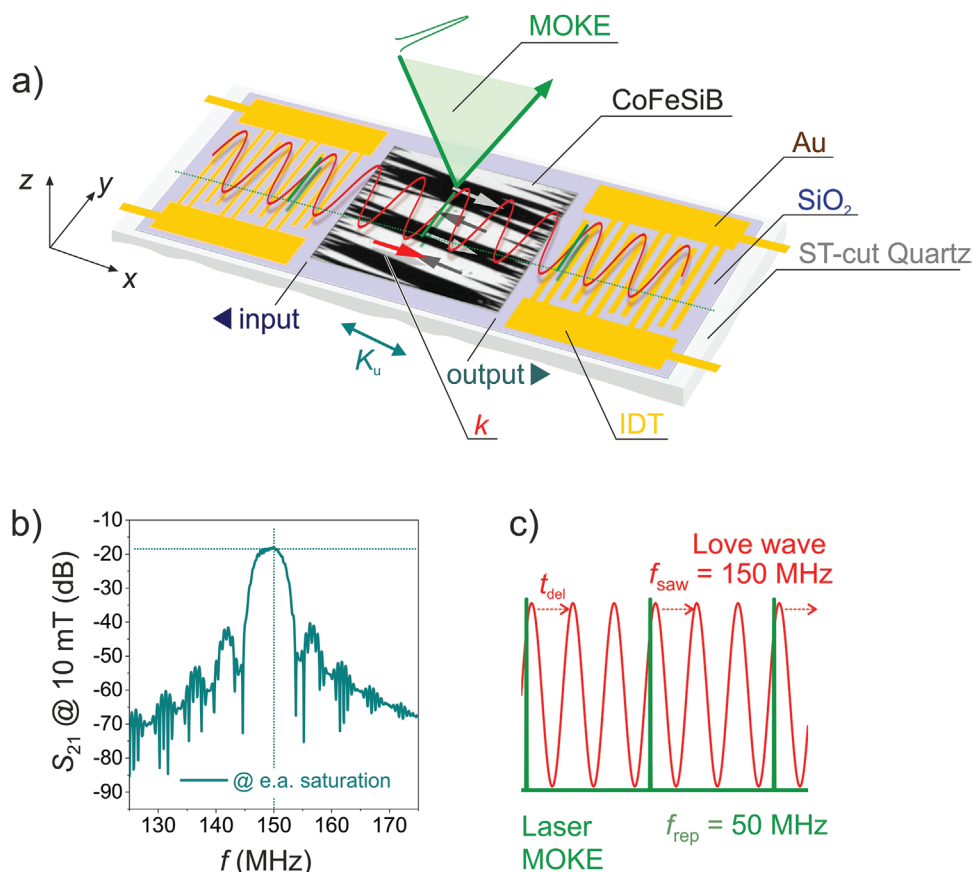


**Figure 1.** a) Scheme of the Love wave based surface acoustic wave delay line sensor device with an ST-cut quartz substrate, an amorphous  $\text{SiO}_2$  guiding layer, and a ferromagnetic magnetostrictive FeCoSiB film forming the delay line between the Au interdigital transducers (IDTs). Shear waves with a wave vector  $k$  (red) are excited in the substrate and the guiding layer by the IDTs, propagating from the input ( $\blacktriangleleft$ ) to the output ( $\blacktriangleright$ ) side. An example zero magnetic field magnetic domain image from the entire ferromagnetic film is depicted. b) Scattering parameter  $S_{21}$  of the SAW device measured at a magnetic saturation field  $\mu_0 H = 10$  mT. The passband of the SAW device centers around three times the Laser repetition rate, where the insertion loss is  $S_{21} \approx -18$  dB. (For the scattering parameters of an equivalent device over a larger frequency range see Supporting Information Figure S1). c) Illumination scheme of phase synchronous stroboscopic time-resolved MOKE microscopy with pulsed laser illumination (green) for operando magnetic imaging (SAW synchronous frequency  $f_{\text{saw}} = 150$  MHz; fixed Laser repetition rate  $f_{\text{rep}} = 50$  MHz) of a Love wave. The phase of the Love wave relative to the Laser pulses is varied in time with a time delay  $t_{\text{del}}$ .

The passband of the SAW magnetic field sensor is centered around  $f_{\text{saw}} = 150$  MHz as seen from the insertion loss data of the SAW device (Figure 1b). The measured insertion loss is solely determined by the SAW device itself.<sup>[28]</sup> Yet, the contributing mechanisms from the magnetic layer are not known. To shed light on the involved magnetic processes, a frequency matching MOKE imaging set-up is adapted for the visualization of the magnetoacoustic wave propagation. The setup is based on a pulsed laser illumination source with a repetition rate of  $f_{\text{rep}} = 50$  MHz.<sup>[49]</sup> By synchronizing the electrical signal at  $f_{\text{saw}} = 150$  MHz with the pulsed laser illumination and by varying the delay  $t_{\text{del}}$  between the electrical signal, respectively the occurring Love waves, and the laser pulses (Figure 1c), stroboscopic magnetic imaging<sup>[49,53]</sup> of the functional magnetic SAW device layer in operation is achieved. The stroboscopic mode allows only for the imaging of repetitive magnetic events in the piezomagnetic layer that occur synchronous with the transduced signal excitation. By this, non-deterministic hysteric and chaotic stochastic magnetic

responses are not directly imaged in the stroboscopically averaged time-resolved imaging.<sup>[54]</sup>

Time-resolved MOKE micrographs from the incoming and outgoing plane wave fronts are shown in Figure 2a. No out-of-plane Rayleigh-like wave response was detected for the SAW device (Supporting Information Figure S3).

Corresponding wave profiles and wave propagation for different time delays are displayed in Figure 2b. The SAW wavelength with the ferromagnetic layer  $\lambda_{\text{fm}}$  is fitted with a sine function to  $\lambda_{\text{fm}} = 272$   $\mu\text{m}$ , which is a reduction from the IDT periodicity of  $\lambda_{\text{IDT}} = 28.0$   $\mu\text{m}$  due to the influence of the magnetostrictive phase, respectively, the corresponding change in phase velocity  $v_p$ . The calculated velocity is  $v_p = \lambda_{\text{fm}} \cdot f_{\text{saw}} = 4080$  m/s. The time-resolved imaging data also allows for the independent extraction of the wave phase velocity (see Supporting Video V1 and V2), which is determined to  $v^+ = 3985$  m/s (Figure 2c) for the wave in forward (+) direction, matching the calculated value within the accuracy of determination. Obviously, the wavelength and phase velocity are reduced to the ferromagnetic phase.

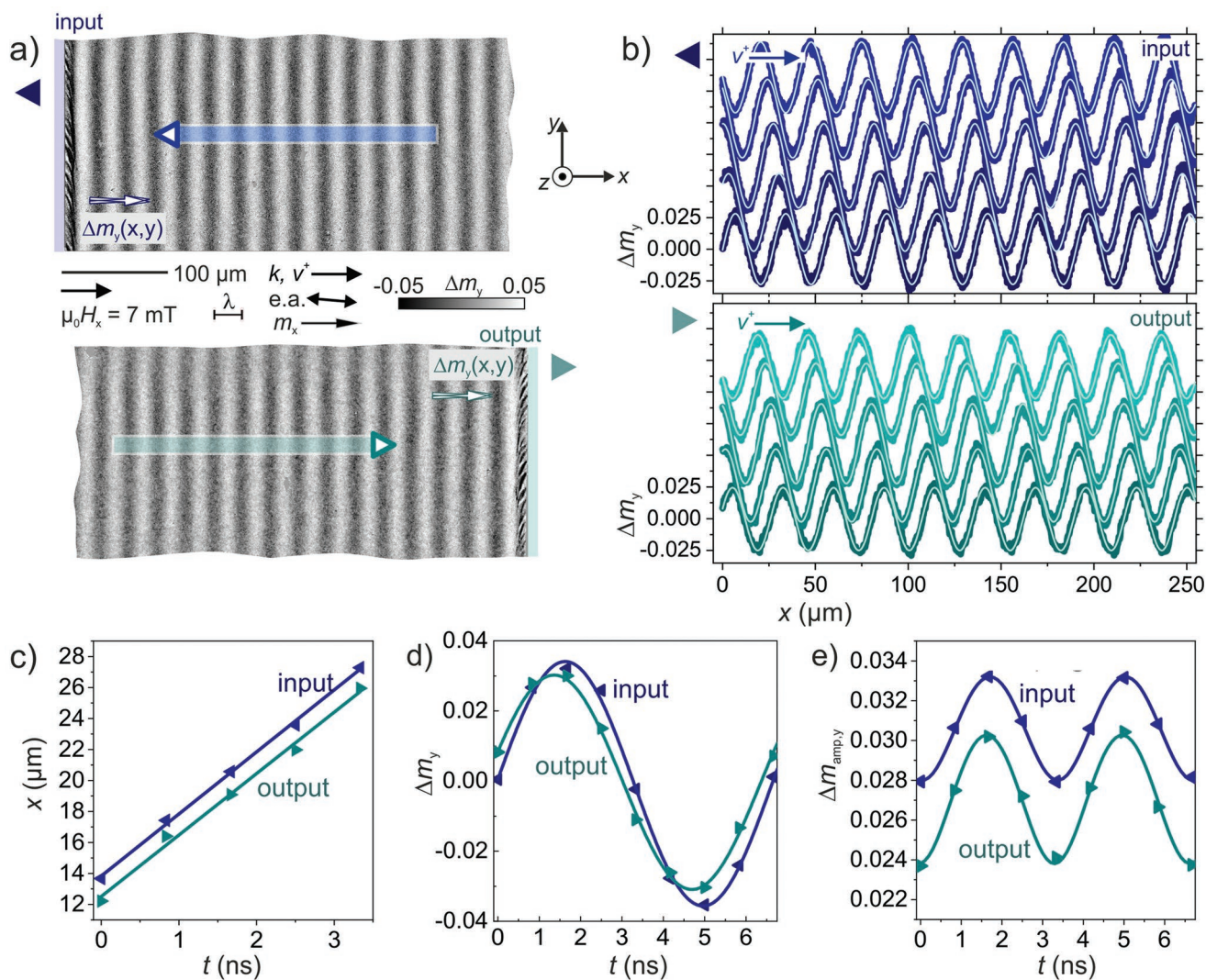


**Figure 2.** a) Snapshots from the dynamic magnetization response  $\Delta m_y (= \Delta M_y/M)$  at the edges of the magnetic film for the incident (side of input,  $\blacktriangleleft$ ) and emerging (side of output,  $\blacktriangleright$ ) shear wave. The direction of propagation of the SAW with a wave velocity  $v^+$  is indicated. A bias magnetic field  $\mu_0 H_x = 7 \text{ mT}$  is applied to align the magnetization parallel to the  $k$  vector. b) Line profiles (positions indicated in a) from snapshots at various points in time ( $t_{\text{del}} = 0\text{--}3.33 \text{ ns}$  from top to bottom) obtained near the edges of the ferromagnetic film. c) Corresponding time difference of the propagating waves. d) Time-evolution of  $\Delta m_y$  at the spatial data points indicated in a) ( $\blacktriangleleft, \blacktriangleright$ ). e) Variation of surface wave amplitudes  $\Delta m_{\text{amp},y}$  over time. The lines correspond to calculated amplitude variations for an interference of forward and reflected waves (see text for details). For the measurements an electrical input power  $P_0 = 10 \text{ dBm}$  was applied to the SAW device.

## 2.2. Wave Reflections

Details on wave propagation across the structured ferromagnetic layer are discussed next. The overall local magnetic response with time of the incident and the emerging wave of the piezomagnetic active element, as indicated in Figure 2a, is shown in Figure 2d. The magnetic input amplitude is slightly higher than the output signal amplitude, indicating that the traveling wave across the delay line damps slightly. Additionally, the overall amplitude of the propagating wave is varying in time at both sides of the patterned FeCoSiB film, which indicates a superposition of two magnetoelastic surface waves of opposite direction of propagation. The resulting wave interference results in the observable amplitude modulation of wave contrast in the time-resolved MOKE images (see Supporting Video V1

and V2). To quantify the magnitudes of the overlapping magnetic waves in the saturated device, we assume two propagating sinusoidal surface waves with opposite wave vectors  $+k$  and  $-k$  for the forward (+) and backward (−) wave propagation. The time dependent amplitude of the surface wave then is

$$\Delta m_y(x, t) = \Delta m_{y+} \cos(k \cdot x - \omega t) + \Delta m_{y-} \cos(-k \cdot x - \omega t) \quad (3)$$

with the time and spatial varying total amplitude  $\Delta m_y$  and the propagating wave amplitudes  $\Delta m_{y+}$  and  $\Delta m_{y-}$ . Comparing the corresponding amplitudes of the incident and emerging waves (Figure 2e), the loss of magnetic wave amplitude across the magnetically saturated ferromagnetic film as well as the reflection and the transmission coefficients at the film edges, respectively, an equivalent to the scattering parameters of magnetic

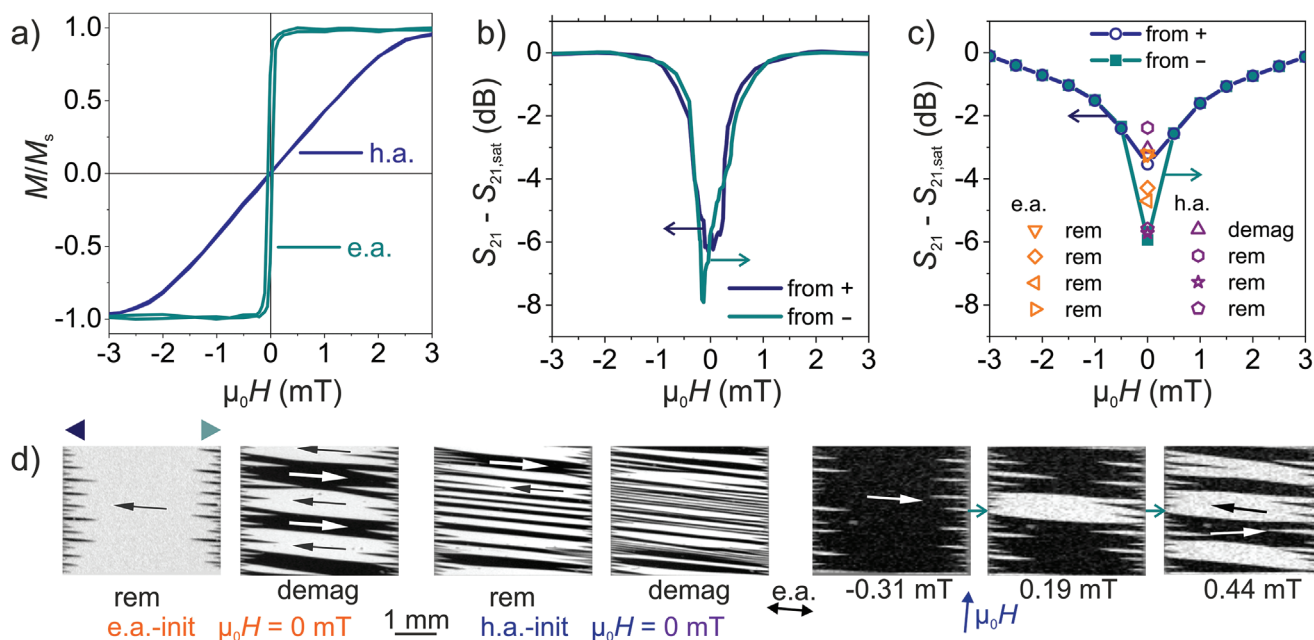


**Figure 3.** a) Magnetization loops from the FeCoSiB film measured along the easy axis (e.a.) and hard axis (h.a.) of anisotropy of the SAW device measured by MOKE magnetometry. b) Magnetic insertion losses  $S_{\text{mag}} (= S_{21} - S_{21,\text{sat}})$  of the SAW magnetic field delay line sensor for a complete magnetization reversal with the applied magnetic field  $\mu_0 H$  approx. along the h.a. of anisotropy. c) Magnetic insertion losses for the magnetization reversal along the e.a. of anisotropy together with insertion losses obtained with different e.a. and h.a. field history at zero magnetic field (rem: remanent magnetic state; demag: demagnetized magnetic state). d) Magnetic micrographs at zero magnetic field after e.a. and h.a. magnetic field applications, and magnetic domain evolution for increasing magnetic fields along the magnetic h.a.. The magnetic field values are indicated. (See also ref. 8 and 28 for comparison). Remanent magnetic states were obtained after e.a. and h.a. magnetic fields of  $\mu_0 H \approx 10$  mT. Demagnetized magnetic states were set by degaussing in a decreasing sinusoidal magnetic field of  $f \approx 10$  Hz starting from  $\mu_0 H \approx 10$  mT.

origin, are derived from the time-resolved imaging data. A similar quantitative analysis by stroboscopic PEEM microscopy of the superposition of propagating SAWs in the piezomagnetic phase was performed in ref. 39. The relative magnetic amplitude transmission across the magnetic film length is  $S_{\text{mag}, \leftarrow} = 0.882$  ( $= -1.1$  dB), respectively the transmission coefficient being  $S_{\text{mag}, \rightarrow} = 0.9656$  mm $^{-1}$  ( $= -0.30$  dB  $\cdot$  mm $^{-1}$ ). These values also represent the maximum conceivable loss in SAW transmission across the length of the ferromagnetic film in the saturated state. Moreover, the wave becomes reflected at the end of the magnetic part of the delay line with the ratio between transmitted and reflected wave  $\Delta m_{y+}/\Delta m_{y-} = 8.44$ , corresponding to a transmission coefficient  $t_{\text{dl}} = 0.88$ , respectively, a reflection coefficient  $r_{\text{dl}} = 0.12$ . The reflected wave naturally leads also to an amplitude modulation at the incoming side of the FeCoSiB film, where we obtain a relative amplitude ratio of the forward and backward moving wave of  $\Delta m_{y+}/\Delta m_{y-} = 11.8$ . The time-varying magnetoelastic response will also be reflected in the overall SAW characteristics.

### 2.3. Magnetic Reversal and Magnetic Losses

During the state of operation, the magnetic sensor is not saturated, and magnetic domains develop. With the introduction of the accompanied magnetic domain walls in the magnetic delay line, additional loss mechanisms arise within the SAW device. The general magnetic response along the easy (e.a.) and hard axis (h.a.) of magnetization together with the

corresponding loss and magnetic domain characteristics are shown in Figure 3.

Comparing the overall magnetization response (Figure 3a) along the magnetic h.a. with the corresponding loss characteristics (Figure 3b), magnetic losses, also hysteretic in nature, become visible in a rather large magnetic field regime. Comparing this to the scattering parameter of the magnetically saturated device, a magnetic scattering parameter of at least  $S_{\text{mag}} = S_{21} - S_{21,\text{sat}} \approx -6$  dB to  $-8$  dB is obtained in the low field regime. Analogous results are attained varying the magnetic field along the e.a. of magnetization, with the magnetic losses scattered from  $S_{\text{mag}} \approx -3$  dB to  $-6$  dB at zero field (Figure 3c). Various values of  $S_{\text{mag}}$  are obtained after different magnetic field histories (as indicated) and are varying in a non-deterministic way. The comparative magnetic domain images display also a varying and non-reproducible magnetic domain structure at and around zero magnetic field for and after h.a. and e.a. field applications. Example domain structures are displayed in Figure 3d (compare to Figure 3b and 3c). 180° magnetic domain walls penetrating the complete magnetic delay line as well as spike domains, entering the sample from the edges, develop. Asymmetries in the magnetic domain structure evolution during h.a. field reversal are also reflected in the hysteretic magnetic behavior of the magnetic losses. By this a connection between the occurrence of magnetic domain walls and the increase of magnetic loss is evidenced. Despite the clear correlation between the increase of losses around zero magnetic field and the manifestation of magnetic domain walls, a further correlation between the details of the actual exhibited magnetic

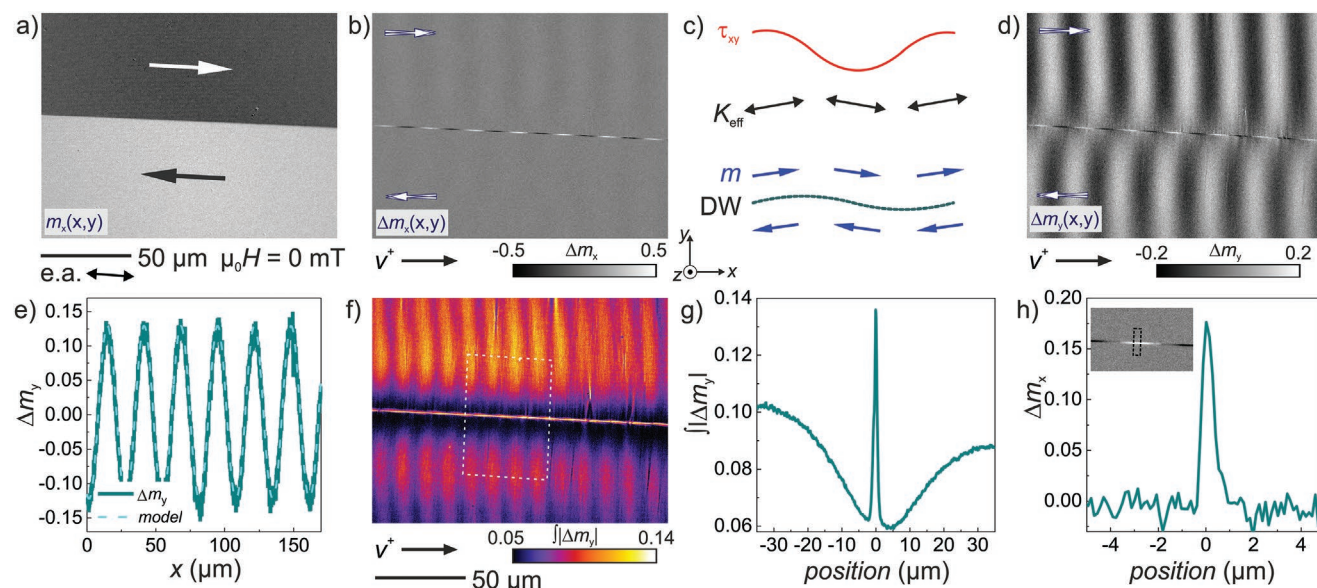


**Figure 4.** a) Quasistatic zero field magnetic domain structure with a 180°-type magnetic domain wall. The main magnetization directions in the magnetic domains are indicated. b) Time-resolved snapshot of  $\Delta m_x$  with the modulated central domain wall (see Supporting Video V3). c) Lateral distribution of  $\tau_{xy}$  with the subsequent modulated effective anisotropy distribution  $K_{\text{eff}}$ , resulting in a modulation of magnetization  $m$  and a correspondingly modulated magnetic domain wall. d) Time-resolved image of  $\Delta m_y$  with the undulated central domain wall for the same phase of excitation as b) (see Supporting Video V4). e) Variation of domain magnetization together with modeled  $\Delta m_y$ . f) Overall magnetization response map  $\int |\Delta m_y(x,y)|$  (equivalent to  $\Delta m_{y,\text{rms}}$ ) and g) variation of  $\Delta m_{y,\text{rms}}$  across the domain wall. h) Asymmetric domain wall response  $\Delta m_x$  (from a). The electrical input power was set to  $P_0 = 10$  dBm.

microstructure at zero field and the actual degree of losses could not be obtained. This points towards local domain wall processes, the mechanism of which is revealed next.

## 2.4. General Magnetic Domain Wall Processes

The correlated magnetic domain wall activity at the synchronous SAW frequency is then clarified by operando magnetic domain observations, beginning with the investigation of a single magnetoelastically excited 180° domain wall. The magnetic domain structure and an analysis of the operando dynamic magnetic domain and domain wall response are shown in Figure 4. The overall static magnetic structure and the corresponding dynamic response characteristics in operation with the MOKE sensitivity parallel to  $k$  in Figure 4a,b reveal a modulated magnetic domain wall response (see also Supporting Video V3) from its static equilibrium position. With the time varying  $\tau_{xy}$  a propagating variation of  $K_{\sigma}$  develops, resulting in the timely variation effective anisotropy  $K_{\text{eff}}$  and alignment of magnetization  $m(t)$  (Figure 4c).

To minimize magnetostatic energy contributions, the domain wall orientation follows the twist in magnetization of the surrounding magnetic matrix (magnetic domains).<sup>[54]</sup> A vibrational modulated 180° domain wall forms. For confirmation, the modulation of magnetization is quantified from the  $\Delta m_y(x,y)$  magnetization response along the y-axis (Figure 4d; Supporting Video V4). Due to the antiparallel magnetization of the magnetic domains a phase shift of  $\pi$  in  $\Delta m_y(x,y)$  occurs across the 180° domain wall (Figure 4d). The change in magnetization is quantified to an amplitude of  $\Delta m_y \approx 0.13$  in the center of the

magnetic domains (Figure 4e) away from the domain wall. This corresponds to a maximum rotation of magnetization by  $\phi_{\text{max}} = \pm 75^\circ$  inside the domains, which closely matches the estimated maximum domain wall tilt  $\phi_{\text{DW,max}} = \pm 8.5^\circ$  of the undulating domain wall seen in Figure 4b,d. Within the accuracy of the measurements, this is in accordance with the arguments laid out above, proving the vibrational domain wall mode is a direct result from the strain-induced modulated magnetization inside the magnetic domains with antiparallel but dynamically modulated magnetization. With the synchronous frequency far below the ferromagnetic resonance of the FeCoSiB film, the amplitude of magnetization response is linear to the excitation and can be obtained by a simple macro-spin model<sup>[55,57]</sup> taking the measured amplitude from the time-resolved magnetic analysis into account (Supporting Information Sect. 1). With  $\lambda_s = 35$  ppm<sup>[58]</sup> and  $K_u = 1330$  J/m<sup>3</sup>, the latter derived from the h.a. magnetization loop, and taking into account  $\Delta m_y$  from the time-resolved MOKE data, we obtain a shear stress amplitude  $\bar{\tau}_{xy} = 3.29$  MPa. The resultant calculated change of magnetization  $\Delta m_y$  with  $\bar{\tau}_{xy}$  is compared to the experimental value in Figure 4e.

Despite the principle agreement of the domain wall response with the central dynamic magnetic excitation, a general reduction of the imaged synchronous magnetization response in the surrounding of the domain wall is observed in Figure 4d. This is in contrast to the analysis of the modulated domain wall angle presented above. Moreover, a minor lower wavelength magnetic contrast modulation is observable at the magnetic domain wall (discussed below). An analysis of the overall imaged dynamic magnetic variation  $\int |\Delta m_y|$ , corresponding to the root mean square response, is shown in Figure 4f,g. From both the

micrograph and the line plot across the domain wall a strong reduction in magnetic contrast over several micrometers away from the domain wall becomes visible. The findings indicate an additional and partly nonreproducible response at the magnetic domain walls. Hence, the drop in magneto-optical contrast of the stroboscopically averaged images is directly attributed to irreversible stochastic magnetization responses, which are out-of-phase with the synchronous SAW frequency and the repetition rate of the laser pulses. From this it follows that a magnetic noise signal is superimposed upon a comparable reproducible magnetization response. On the other hand, the existence of a full amplitude magnetization response is proved from the maximum magnetic domain wall alignment discussed above. This discrepancy is a further proof of domain wall mediated magnetic noise. The drop in synchronous magnetic response is asymmetric around the magnetic domain wall, which we attribute to an unbalanced domain wall action due to the asymmetric Bloch wall structure.<sup>[55]</sup> The overall behavior indicates the occurrence of magnetic domain wall resonances. For similar amorphous magnetic films<sup>[59]</sup> and FeCoSiB films,<sup>[60,61]</sup> magnetic field driven domain wall resonance effects in the lower hundreds MHz regime have been reported, also connected to

the magnetic losses. Eddy-current effects at the asymmetric Bloch walls do not play a role for the given frequency and FeCoSiB film thickness.<sup>[62,63]</sup> A further proof of the asymmetry and of a fluctuation of the domain wall response characteristics is shown in Figure 4h, displaying a snapshot of the likewise asymmetric course of  $\Delta m_x$  across the magnetic domain wall (compare to Figure 4b). One side of the domain wall is blurred in the magnetization response images, furthermore indicating irreversible or non-reproducible domain wall responses, and by this contributing to magnetic (phase) noise during sensor operation.

## 2.5. Magnetic Domain Wall Transitions

The origin of the additionally observed smaller wavelength wave propagation at the domain wall from a magnetic domain wall transition, a single magnetic Bloch line, is demonstrated in Figure 5. Figure 5a shows the quasistatic magnetic domain structure and Figure 5b the dynamic magnetization response  $\Delta m_y$ .

Similar magnetization waves propagating along 180° asymmetric Bloch domain walls<sup>[55]</sup> have been reported for

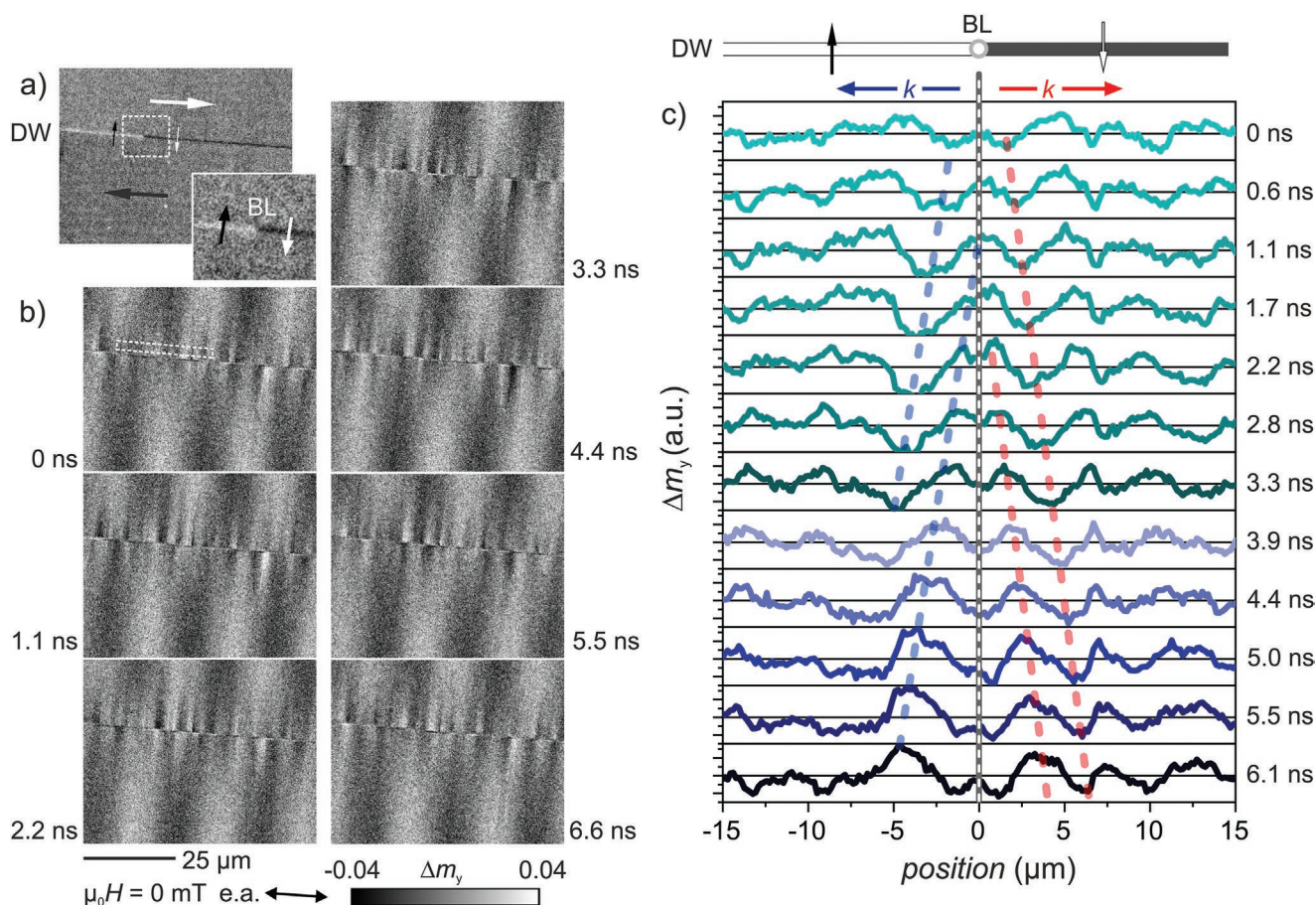


**Figure 5.** a) Quasistatic zero field magnetic domain structure with a 180° asymmetric domain wall and a Bloch line (BL) visible from the alteration of the magnetic domain wall contrast. The main magnetization directions inside the magnetic domains and at the domain wall are indicated. b) Time-resolved sequence of  $\Delta m_y$  (see Supporting Video V5). c) Line profiles from Fourier filtered domain micrographs at various points in time ( $t_{\text{del}} = 0\text{--}6.1$  ns) obtained in the vicinity of the magnetic domain wall with a Bloch line (investigated area indicated in Figure 5b, for the full process see Supporting Video V6). The Bloch line position is indicated. The electrical input power was  $P_0 = 10$  dBm.

magnetic field excited magnetic domain walls in almost identical FeCoSiB films.<sup>[61]</sup> There, the wave generation is related to oscillating magnetic closure domain walls in magnetic elements, which for topological reasons also exhibit at least one Bloch line at the closure domain or within the magnetic domain wall. Analogously, magnetic domain mediated magnetization wave generation, now magnetoelastic in origin, occurs from the magnetic transition inside the wall as the vortex-like Bloch line in the thin film imposes different magnetic boundary conditions in its vicinity and, thus, disturbs the local magnetization response. The local effective magnetoelastic field drives the inhomogeneous spin system, which enables the generation of spin waves confined to the domain wall structure.<sup>[64]</sup> We believe that any magnetic or structural defect, and magnetic pinning sites will act in a similar way on the domain wall as the Bloch lines.

Line plots of wave propagation obtained from band-stop filtered images are displayed in Figure 5c (the region of extraction is indicated in Figure 5b at 0 ns). The waves propagate oppositely from both sides of the Bloch line. A precise determination of the wave velocity is not feasible, but from the line plots we approximate a magnitude of phase velocity below  $v_{p,DW} \approx \pm 1000$  m/s, a value which is significantly smaller than the SAW phase velocity. The data suggests an additional strong impact from magnetic domain walls and domain wall details on SAW propagation.

## 2.6. Spike Domain Structures

The complex interactions of SAWs with more complex magnetic domain structures that naturally form at the edges of the magnetic delay line in the magnetic unsaturated state are shown in Figure 6 for incident and emerging SAWs.

The wave field distribution for the incoming waves shows a strong impact from the magnetic domain structure on the SAW distribution. Small wavelength excitations at the magnetic domain walls as well as a strong reduction of the synchronous wave inside the spike domains are revealed (Figure 6a, Supporting Video V7). A shift and a tilting in the magnetoacoustic wave front due to the tilting of magnetization inside the magnetic domains and due to the occurrence of the magnetic domain walls appear (see also Supporting Information Figure S4). The domain structure leads to a hindered synchronous magnetic response more than 100  $\mu\text{m}$  away from the beginning of the magnetic delay line. The quantitative analysis of the total dynamic magnetic variation (Figure 6b) with the synchronous amplitude reduction again points to irreversible magnetization response at the magnetic domain structure. A similar magnetic response reduction occurs in the vicinity of the central 180° domain wall as discussed before. From the irreversible response in the magnetic sensing layer, we again deduce a strong contribution to magnetic noise. Similar response characteristics are also found at the end of the magnetic delay line (Figure 6c,d, Supporting Video V8). The same conclusion as discussed above can be drawn from the magnetic wave patterns, now for the outgoing SAW. Yet, additional wave reflections from the spike domain structure occur, e.g., detectable from a modulation of the magnetic wave in time. Corresponding wave profiles and

wave propagation for different time delays are displayed in Figure 6e (from the region marked in Figure 6c).

The magnetoelastic response in front of the spike domain can be fitted to a sine function with  $\lambda_{fm} \approx 270$   $\mu\text{m}$ , but with strongly varying amplitude from  $\Delta m_{y,min} = 0.033$  to  $\Delta m_{y,max} = 0.071$ , which implies the interference of two magnetoacoustic waves of opposing direction of propagation. Apparently, the wave incident on the spike domain is partially reflected. For the shown example, this corresponds to a transmission coefficient  $t_{dl} = 0.56$ , respectively, a reflection coefficient  $r_{dl} = 0.44$ . This reflection coefficient is significantly above the reflection from the structural edge in the saturated magnetization state. To demonstrate the differences in characteristics of a SAW passing through and SAW reflections at a magnetic domain structure, we investigated the very same domain structure for an incoming (Figure 6f, Supporting Video V9) and outgoing (Figure 6g; Supporting Video V10) SAW. The wave pattern is nearly undisturbed for the case of  $v^-$  and wave transmission (indicated by a straight line in Figure 6f). In contrast to that, for the waves propagating with  $v^+$  the reflections lead to a significant modulation in magnetic wave amplitude, but also to an additional wave distortion (indicated by the bended line in the top domain in Figure 6g) that changes in time. The corresponding variations in phase with time for the region below and close to the spike domain point are shown in Figure 6h. The distortion and the amplitude variations are once more indicating magnetic domain wall interactions, resulting in SAW propagation disturbance that will contribute to uncorrelated magnetic noise during sensor operation.

## 3. Conclusions

Using time-resolved magneto-optical microscopy, the principle observation of purely in-plane Love wave propagation in magnetoelectric SAW devices on plane surfaces is demonstrated. The wide-field method is based on the application of magnetic layers and contrast generation through magnetic circular birefringence, respectively, the magneto-optical Kerr effect. The principle is adaptable to SAW devices without magnetic layers with optical contrast generation and based on linear birefringence for the imaging of propagating shear waves.

In the SAW magnetic field sensor devices, we uncovered strong interactions between details of the magnetic domain structure and the propagating magnetoacoustic waves. The magnetoacoustic shear waves display signatures of wave bending and reflections on structural and micromagnetic features, leading to spatially and temporally varying alterations of the propagating waves. Additional complex vibrational domain wall modes with extra wave propagation along the magnetic domain walls are found, which are a direct consequence of micromagnetic variations inside the magnetic domain walls. The spatially distributed loss of wave amplitude in the synchronous detection scheme is traced back to asynchronous or stochastic dynamic magnetization responses, also indicating magnetic domain wall resonance effects. We identify the additional and uncorrelated magnetization answer at and off the domain walls as the main source of magnetic noise exhibited in magnetic sensor operation.

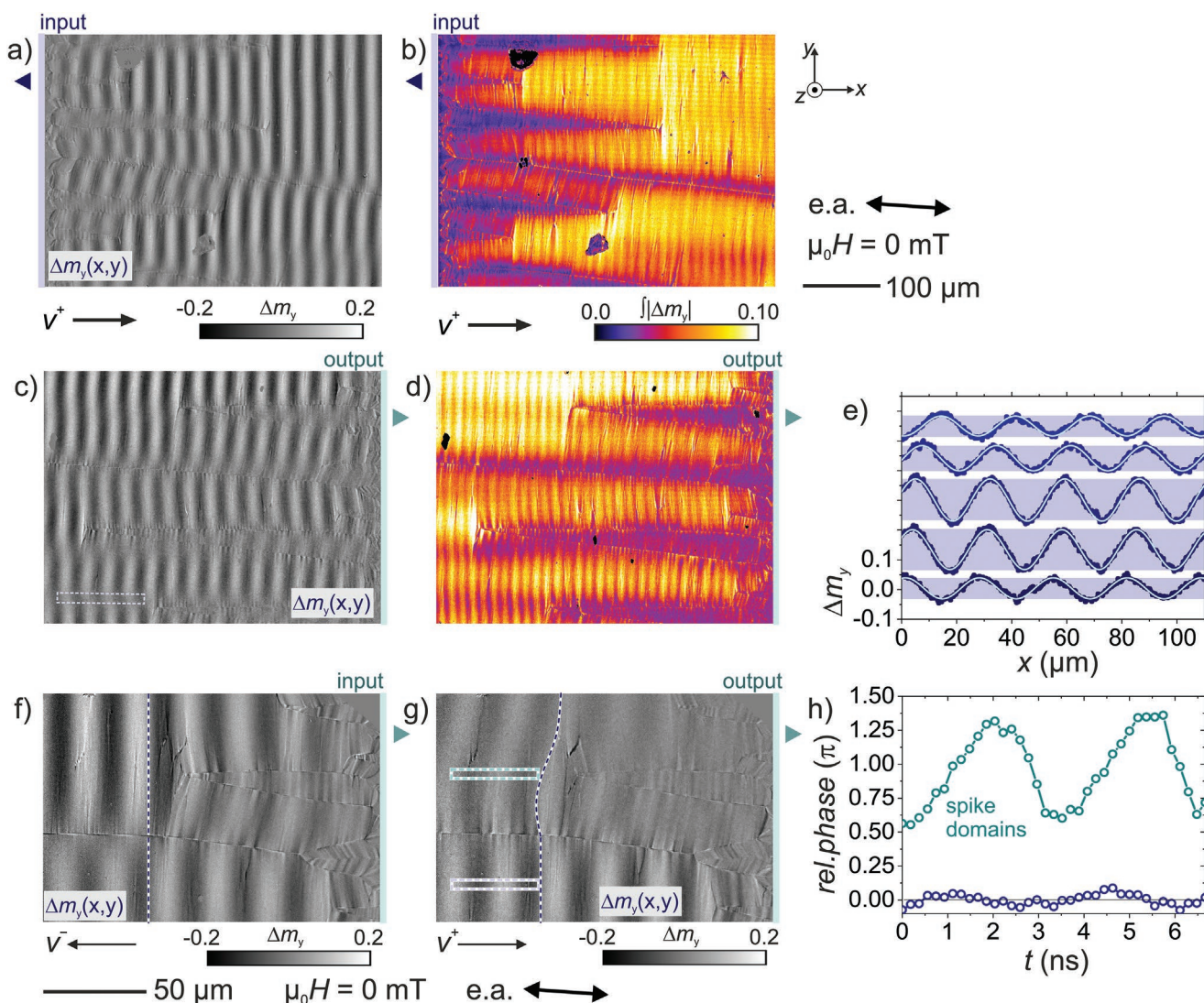


**Figure 6.** a) Time-resolved snapshot of  $\Delta m_y$  of the incident wave (input,  $\blacktriangleleft$ ) of the magnetic film for the shear wave with magnetic spikes domains and a  $180^\circ$  magnetic domain wall structure (see Supporting Video V7). b) Overall magnetization response map  $\int |\Delta m_y(x,y)|$  corresponding to the process shown in a). c) Snapshot of  $\Delta m_y$  of the emerging wave of the delay line (output,  $\blacktriangleright$ ) of the magnetic film for the outgoing shear wave (Supporting Video V8). d) Magnetization response map  $\int |\Delta m_y(x,y)|$  corresponding to c). e) Variation of  $\Delta m_y$  with time in front of the spike domain ( $t_{\text{del}} = 0\text{--}3.33$  ns). The region of data extraction is indicated in c). The wave amplitude is color coded for better visibility. f)  $\Delta m_y$  for the (now) incident wave (input,  $\blacktriangleleft$ ,  $v^-$ ) (see Supporting Video V9) and g) the outgoing wave of the delay line (output,  $\blacktriangleright$ ,  $v^+$ ) (see Supporting Video V10) for the same location and the equal underlying magnetic domain structure. h) Relative phase variation in the bottom magnetic domain and in front of the spike domain structure. The regions of wave analysis are indicated in g). The electrical input power was  $P_0 = 10$  dBm.

The obtained data points to the reduction or even elimination of spin textures for ideally performing future magnetoelectric Love wave sensor devices. Introducing magnetic multilayers for magnetic domain wall elimination, e.g., with antiparallel exchange bias,<sup>[65]</sup> seems the most promising way for such a sensor improvement. Eliminating magnetic closure domains by a non-colinear alignment of the magnetic anisotropy relative to the edges or magnetic sensing modes with non-colinear magnetic field applications should result in a similar improvement in magnetic noise. Varying the structures to apply fundamental frequencies beyond the domain wall resonance, will diminish the domain wall contributions. From a structural point of view, introducing tapered edges

of the magnetic structure, wave reflections would be attenuated. Furthermore, and most importantly, due to the correspondingly accompanying reduction in the magnetostatic energy contributions, the closure domain structures would be reduced.

Overall, we show that the control of magnetic domains and magnetic domain walls are key for improved magnetoelectric magnetic field sensors with low limit of detection. The purely magnetoelastic mechanisms of magnetic noise generations are determined. Advanced spatial and time-resolved operando characterization techniques for the identification of the mechanisms that limit device performances are most crucial for sensor improvements.

## 4. Experimental Section

**SAW Device:** The SAW device consists of a 4.6 mm long delay line on top of a 500  $\mu\text{m}$  thick ST-cut quartz substrate ( $42^\circ 45'$  Y-cut) to excite the shear waves, propagating orthogonally to the crystallographic  $x$ -axis.<sup>[8,66]</sup> The delay line is formed by two split finger interdigital transducer (IDT) electrodes, each finger 3.5  $\mu\text{m}$  wide and with a periodicity  $p = 28 \mu\text{m}$ . The split finger interdigital transducers are used to eliminate strip edge reflections. The electrodes are formed from Cr/Au/Cr (12 nm/300 nm/12 nm thick). The delay line and the IDT electrodes are covered by an amorphous  $\text{SiO}_2$  layer (4.5  $\mu\text{m}$  thick), which acts as a guiding layer due to the lower shear velocity compared to the quartz substrate. Between the IDT structures a soft-magnetic amorphous Ta/( $\text{Fe}_{90}\text{Co}_{10}$ )<sub>78</sub> $\text{Si}_{12}\text{B}_{10}$ /Ta (10 nm/200 nm/10 nm thick) film is deposited by rf magnetron sputtering. To induce a magnetic anisotropy along the axis of wave propagation, a dc magnetic field ( $\mu_0 H_{\text{dep}} = 10 \text{ mT}$ ) is applied during film deposition.<sup>[8,17]</sup> The saturation magnetization of ( $\text{Fe}_{90}\text{Co}_{10}$ )<sub>78</sub> $\text{Si}_{12}\text{B}_{10}$  is  $\mu_0 M_s = 1.5 \text{ T}$ <sup>[58]</sup> and the saturation magnetostriction is  $\lambda_s \approx 35 \cdot 10^{-6}$ .<sup>[47]</sup> The magnetic film is structured by lift-off lithography with a length  $l = 3.8 \text{ mm}$  along the wave vector.

**Electrical Characterization:** Two-port scattering parameters of the sensor are measured with a calibrated vector network analyzer. To minimize mismatch losses due to reflections at the electrical-acoustical interfaces, an individual impedance matching to the system impedance ( $Z_0 = 50 \Omega$ ) was implemented using discrete inductors and capacitors.<sup>[67]</sup> Magnetic fields were applied along and perpendicular to the determined easy and hard axis of magnetization for the magnetic domain experiments.

**Quasistatic Magnetic Characterization:** For the general magnetic film characterization, magnetooptical Kerr effect (MOKE) magnetometry and quasistatic magnetic domain imaging were performed with a home-built large-view MOKE setup with telecentric lens optics.<sup>[49,53]</sup> The system is equipped with Helmholtz coils and an electromagnet for magnetic field application. Prior to the electrical characterizations with different magnetic field history, the magnetic domain states were set in the MOKE microscopy setup. After the electrical characterizations the magnetic domain states were checked again by large-view MOKE microscopy.

**In Situ Time-Resolved Magnetic Imaging:** Time-resolved imaging experiments are performed in a time-resolved wide-field magnetooptical Kerr microscope, which utilizes stroboscopic magnetic imaging with a pulsed laser that has a repetition rate of  $f_{\text{rep}} = 50 \text{ MHz}$ , a pulse width of  $p\omega = 7 \text{ ps}$ , and a wavelength of  $\lambda = 532 \text{ nm}$ .<sup>[39–41]</sup> The laser pulse width corresponds to a bandwidth of  $bw \approx 50 \text{ GHz}$  for the imaging system. The spatial resolution limits the detection of SAWs to minimum wavelengths of about 500 nm.

The illuminating pulsed laser is phase-locked to a signal generator ( $Z_0 = 50 \Omega$ ) exciting SAWs at a frequency of  $f_{\text{SAW}} = 150 \text{ MHz}$  via the IDTs, utilizing stroboscopic illumination for time-resolved microscopy. The SAW device in operation is illuminated under perpendicular or oblique plane of incidence, resulting in a polar (out-of-plane) or longitudinal (in-plane) magnetooptical contrast.<sup>[55]</sup> To quantify the magnetic response to an external excitation, the magnetization is saturated by a static external field in different azimuthal angles and the resulting image contrast is fitted to a sensitivity curve for calibration.<sup>[68,51]</sup> During the time-resolved imaging, variable magnetic bias fields under different angles relative to the direction of wave propagation can be applied using a freely rotatable electromagnet.

## Supporting Information

Supporting Information is available from the Wiley Online Library or from the author.

## Acknowledgements

This work was supported by the German Research Foundation (Deutsche Forschungsgemeinschaft, DFG) through the Collaborative

Research Centre CRC 1261 “Magnetolectric Sensors: From Composite Materials to Biomagnetic Diagnostics”. The authors acknowledge A. Winkler from the IFW Dresden for the vibrometry measurements. J. M. thanks J. Schmalz for stimulating discussions and for sharing COMSOL simulation data. Further thanks go to Elizaveta Golubeva for data extraction. The authors also thank K. Brandenburg and S. Paulsen-McCord for proofreading of the manuscript.

Open access funding enabled and organized by Projekt DEAL.

## Conflict of Interest

The authors declare no conflict of interest.

## Data Availability Statement

The data that support the findings of this study are available from the corresponding author upon reasonable request.

## Keywords

Kerr microscopy, magnetic domains, magnetic field sensors, magnetolectric composites, surface acoustic waves

Received: January 8, 2022

Revised: April 9, 2022

Published online: May 4, 2022

- [1] A. Edelstein, *J. Phys.: Cond. Mater.* **2007**, *19*, 165217.
- [2] C. Zheng, K. Zhu, S. C. De Freitas, J. Y. Chang, J. E. Davies, P. Eames, P. P. Freitas, O. Kazakova, C. Kim, C. W. Leung, S. H. Liou, *IEEE Trans. Magn.* **2019**, *5*, 0800130.
- [3] E. Ramsden, *Hall-Effect Sensors: Theory and Application*, Elsevier, Newnes, Boston, USA **2006**.
- [4] Y. Wang, D. Gray, D. Berry, J. Gao, M. Li, J. Li, D. Viehland, *Adv. Mater.* **2011**, *23*, 4111.
- [5] D. Viehland, M. Wuttig, J. McCord, E. Quandt, *MRS Bull.* **2018**, *43*, 834.
- [6] M. Inoue, S. Yamamoto, N. Fujita, T. Fujii, *IEEE Trans. Magn.* **1987**, *23*, 3334.
- [7] M. Elhosni, O. Elmazria, S. Petit-Watelot, L. Bouvot, S. Zhgoon, A. Talbi, M. Hehn, K. A. Aissa, S. Hage-Ali, D. Lacour, F. Sarry, O. Boumatar, *Sens. Actuators, A* **2016**, *240*, 41.
- [8] A. Kittmann, P. Durdaut, S. Zabel, J. Reermann, J. Schmalz, B. Spetzler, D. Meyners, N. X. Sun, J. McCord, M. Gerken, G. Schmidt, M. Höft, R. Knöchel, F. Faupel, E. Quandt, *Sci. Rep.* **2018**, *8*, 278.
- [9] M. J. Vellekoop, *Ultrasonics* **1998**, *36*, 7.
- [10] B. Drafts, *IEEE Trans. Microwave Theory Tech.* **2001**, *49*, 795.
- [11] D. Mandal, S. Banerjee, *Sensors* **2022**, *22*, 820.
- [12] M. D. Schlensog, T. M. A. Gronewold, M. Tewes, M. Farnulok, E. Quandt, *Sens. Actuators, B* **2016**, *101*, 308.
- [13] M.-I. Rocha-Gaso, C. March-Iborra, Á. Montoya-Baides, A. Arnau-Vives, *Sensors* **2009**, *9*, 5740.
- [14] Z. Xu, Y. J. Yuan, *Biosens. Bioelectron.* **2018**, *99*, 500.
- [15] H. Zhou, A. Talbi, N. Tiercelin, O. Bou Matar, *Appl. Phys. Lett.* **2014**, *104*, 114101.
- [16] J. Y. Duquesne, P. Rovillain, C. Hepburn, M. Eddrief, P. Atkinson, A. Anane, R. Ranchal, M. Marangolo, *Phys. Rev. Appl.* **2019**, *12*, 024042.
- [17] V. Schell, C. Müller, P. Durdaut, A. Kittmann, L. Thormählen, F. Lofink, D. Meyners, M. Höft, J. McCord, E. Quandt, *Appl. Phys. Lett.* **2020**, *116*, 073503.

- [18] H. Mishra, M. Hehn, S. Hage-Ali, S. Petit-Watlot, P. W. Mengue, S. Zghoon, H. M'jahed, D. Lacour, O. Elmazria, *Phys. Rev. Appl.* **2020**, 14, 014053.
- [19] A. Mazzamurro, Y. Dusch, P. Pernod, O. Bou Matar, A. Addad, A. Talbi, N. Tiercelin, *Phys. Rev. Appl.* **2020**, 13, 210903.
- [20] D. C. Webb, D. W. Forester, A. K. Ganguly, C. Vittoria, *IEEE Trans. Magn.* **1979**, 15, 1410.
- [21] B. S. Berry, W. C. Pritchett, *J. Appl. Phys.* **1976**, 47, 3295.
- [22] C. Tsang, S. K. Decker, *J. Appl. Phys.* **1981**, 52, 2465.
- [23] L. Jiang, E. R. Nowak, P. E. Scott, J. Johnson, J. M. Slaughter, J. J. Sun, R. W. Dave, *Phys. Rev. B* **2004**, 69, 054407.
- [24] M. Xiao, K. B. Klaassen, J. C. van Peppen, M. H. Kryder, *J. Appl. Phys.* **1999**, 85, 5855.
- [25] R. Kubo, *Rep. Prog. Phys.* **1966**, 29, 255.
- [26] H. T. Hardner, M. B. Weissman, M. B. Salamon, S. S. P. Parkin, *Phys. Rev. B* **1993**, 48, 16156.
- [27] N. Smith, P. Arnett, *Appl. Phys. Lett.* **2001**, 78, 1448.
- [28] P. Durdaut, C. Müller, A. Kittmann, V. Schell, A. Bahr, E. Quandt, R. Knöchel, M. Höft, J. McCord, *Sensors* **2021**, 21, 5631.
- [29] A. Kittmann, C. Müller, P. Durdaut, L. Thormählen, V. Schell, F. Niekkel, F. Lofink, D. Meyners, R. Knöchel, M. Höft, J. McCord, E. Quandt, *Sens. Actuators, A* **2020**, 311, 111998.
- [30] N. O. Urs, E. Golubeva, V. Röbisch, S. Toxvaerd, S. Deldar, R. Knöchel, M. Höft, E. Quandt, D. Meyners, J. McCord, *Phys. Rev. Appl.* **2020**, 13, 024018.
- [31] P. Hayes, M. Jovičević Klug, S. Toxvaerd, P. Durdaut, V. Schell, A. Teplyuk, D. Burdin, A. Winkler, R. Weser, Y. Fetisov, M. Höft, R. Knöchel, J. McCord, E. Quandt, *Sci. Rep.* **2019**, 9, 16355.
- [32] A. A. Maznev, A. M. Lomonosov, P. Hess, A. A. Kolomenskii, *Eur. Phys. J. B* **2003**, 35, 429.
- [33] O. B. Wright, O. Matsuda, *Philos. Trans. R. Soc. A Math. Phys. Eng. Sci.* **2015**, 373, 20140364.
- [34] K. Nakano, K. Hane, S. Okuma, T. Eguchi, *Opt. Rev.* **1997**, 4, 265.
- [35] T. Tachizaki, T. Muroya, O. Matsuda, Y. Sugawara, D. H. Hurley, O. B. Wright, *Rev. Sci. Instrum.* **2006**, 77, 043713.
- [36] J. L. Blackshire, S. Sathish, B. D. Duncan, M. Millard, *Opt. Lett.* **2002**, 27, 1025.
- [37] L. Zheng, D. Wu, X. Wu, K. Lai, *Phys. Rev. Appl.* **2018**, 9, 061002.
- [38] M. Foerster, F. Macià, N. Statuto, S. Finizio, A. Hernández-Mínguez, S. Lendínez, P. V. Santos, J. Fontcuberta, J. M. Hernández, M. Kläui, L. Aballe, *Nat. Commun.* **2017**, 8, 407.
- [39] M. Foerster, N. Statuto, B. Casals, A. Hernández-Mínguez, S. Finizio, A. Mandziak, L. Aballe, J. M. Hernández Ferràs, F. Macià, *J. Synchrotron Radiat.* **2019**, 26, 184.
- [40] N. Smagin, L. Djoumi, E. Herth, M. Vanotti, D. Fall, V. Blondeau-Patissier, M. Duquennoy, M. Ouafouh, *Sens. Actuators, A* **2017**, 264, 96.
- [41] T. Saito, O. Matsuda, M. Tomoda, O. B. Wright, *J. Opt. Soc. Am. B* **2010**, 27, 2632.
- [42] A. Miyamoto, S. Matsuda, S. Wakana, A. Ito, *Electron. Commun. Japan, Part II Electron.* **2004**, 87, 10.
- [43] P. Kuszewski, J. Y. Duquesne, L. Becerra, A. Lemaître, S. Vincent, S. Majrab, F. Margaillan, C. Gourdon, L. Thevenard, *Phys. Rev. Appl.* **2018**, 10, 034036.
- [44] B. Casals, N. Statuto, M. Foerster, A. Hernández-Mínguez, R. Cicheler, P. Manshausen, A. Mandziak, L. Aballe, J. M. Hern, F. Maci, *Phys. Rev. Lett.* **2020**, 124, 137202.
- [45] Y. Li, C. Zhao, W. Zhang, A. Hoffmann, V. Novosad, *APL Mater.* **2021**, 9, 060902.
- [46] D. A. Bozhko, V. I. Vasyuchka, A. V. Chumak, A. A. Serga, *Low Temp. Phys.* **2020**, 46, 383.
- [47] N. K. P. Babu, A. Trzaskowska, P. Graczyk, G. Centała, S. Mieszczyk, H. Głowiński, M. Zdunek, S. Mielcarek, J. W. Kłos, *Nano Lett.* **2021**, 21, 946.
- [48] K. Yamamoto, M. Xu, J. Puebla, Y. Otani, S. Maekawa, *J. Magn. Magn. Mat.* **2022**, 545, 168672.
- [49] J. McCord, *J. Phys. D: Appl. Phys.* **2015**, 48, 333001.
- [50] B. Mozooni, T. von Hofe, J. McCord, *Phys. Rev. B* **2014**, 90, 9.
- [51] R. B. Holländer, C. Müller, M. Lohmann, B. Mozooni, J. McCord, *J. Magn. Magn. Mater.* **2017**, 432, 283.
- [52] M. R. Freeman, W. K. Hiebert, A. Stankiewicz, *J. Appl. Phys.* **1998**, 83, 6217.
- [53] N. O. Urs, B. Mozooni, P. Mazalski, M. Kustov, P. Hayes, S. Deldar, E. Quandt, J. McCord, *AIP Adv.* **2016**, 6, 055605.
- [54] M. R. Freeman, R. W. Hunt, G. M. Steeves, *Appl. Phys. Lett.* **2000**, 77, 717.
- [55] A. Hubert, R. Schäfer, *Magnetic Domains*, Springer, Berlin, Germany **2009**.
- [56] E. C. Stoner, E. P. Wohlfarth, *Philos. Trans. R. Soc. A Math. Phys. Eng. Sci.* **1948**, 240, 599.
- [57] L. Dreher, M. Weiler, M. Pernpeintner, H. Huebl, R. Gross, M. S. Brandt, S. T. B. Goennenwein, *Phys. Rev. B* **2012**, 86, 134415.
- [58] A. Ludwig, E. Quandt, *IEEE Trans. Magn.* **2002**, 38, 2829.
- [59] U. Queitsch, J. McCord, A. Neudert, R. Schäfer, L. Schultz, K. Rott, H. Brückl, *J. Appl. Phys.* **2006**, 100, 093911.
- [60] B. Mozooni, T. von Hofe, J. McCord, *Phys. Rev. B* **2014**, 90, 054410.
- [61] B. Mozooni, J. McCord, *Appl. Phys. Lett.* **2015**, 107, 042402.
- [62] A. Aharoni, J. Jakubovics, *Philos. Mag. B* **1982**, 46, 253.
- [63] S. W. Yuan, H. N. Bertram, *IEEE Trans. Magn.* **1993**, 29, 2515.
- [64] E. Schlömann, R. I. Joseph, *J. Appl. Phys.* **1964**, 35, 2382.
- [65] M. J. Klug, L. Thormählen, V. Röbisch, S. D. Toxvaerd, M. Höft, R. Knöchel, E. Quandt, D. Meyners, J. McCord, *Appl. Phys. Lett.* **2019**, 114, 192410.
- [66] B. Jakoby, M. J. Vellekoop, *Smart Mater. Struct.* **1997**, 6, 668.
- [67] P. Durdaut, A. Kittmann, E. Rubiola, J.-M. Friedt, E. Quandt, R. Knöchel, M. Höft, *IEEE Sens. J.* **2019**, 19, 8000.
- [68] W. Rave, A. Hubert, *IEEE Trans. Magn.* **1990**, 26, 2813.